Applied Catalysis B: Environmental 339 (2023) 123172

Contents lists available at ScienceDirect

Applied Catalysis B: Environmental

journal homepage: www.elsevier.com/locate/apcatb

Fe phthalocyanine stabilized on phosphorous-doped multi-defective carbon nanoribbons as oxygen reduction electrocatalysts

Qi Huang [a,c,1], Shaojie Xu [a,1], Jie Liu [a,1], Yuanyuan Guo [a], Dandan Chen [a], Qiuhong Sun [a], Linjie Zhang [b], Huagui Nie [a], Zhi Yang [a,*], Jinjie Qian [a,*]

[a] Key Laboratory of Carbon Materials of Zhejiang Province, College of Chemistry and Materials Engineering, Wenzhou University, Wenzhou 325000, PR China
[b] State Key Laboratory of Structural Chemistry, Fujian Institute of Research on the Structure of Matter, Chinese Academy of Sciences, Fuzhou 350002, PR China
[c] State Key Laboratory of Materials Processing and Die & Mould Technology, School of Materials Science and Engineering, Huazhong University of Science and Technology, Wuhan 430074, PR China

ARTICLE INFO

Keywords:
Coordination polymer
Carbon nanoribbon
Iron phthalocyanine
Oxygen reduction
Zn-air battery

ABSTRACT

Coordination polymers can be utilized as ideal precursors due to their ability to change their growth behavior and topological structure through solvent-induced effects. In this work, nanostrip-like crystalline particles, transformed from interchangeable indium-based coordination polymers (**InOF-25/26**), are treated to synthesize phosphorus-doped multi-defective carbon nanoribbons for efficiently anchoring iron phthalocyanine. The obtained **FePc-Fe_2P@25-CNR** electrocatalyst exhibits a superior half-wave potential of 0.899 V and a large diffusion current density of 5.152 mA cm^{-2} in oxygen reduction reaction (ORR). Meanwhile, it also shows excellent stability in homemade Zn-air batteries with satisfactory charge/discharge durability over 100 cycles. In this case, the ORR performance can be improved by phosphating the carbon surface, reinforcing tight bonding with transition metal phthalocyanines, and inducing charge migration to increase the electrocatalysis kinetics, which is further validated by relevant theoretical calculation. This synthetic strategy combines structurally variable coordination polymers with metallomacrocyclic molecules, exploiting a feasible pathway for the preparation of high-performance electrochemical catalysts.

1. Introduction

In order to expedite the achievement of carbon neutrality, the development of sustainable and environmentally friendly fuel cells has become a major focus to substitute traditional fossil fuels as energy sources [1]. Among various types of fuel cells, proton exchange membrane fuel cell is composed of a fuel electrode, air electrode, and electrolyte, and operates on the fundamental principle of redox reactions [2]. Generally speaking, the oxygen reduction reaction (ORR) mainly takes place at the air electrode, and it requires high-performance and practical four-electron ORR catalysts to improve the overall efficiency of the fuel cells [3,4]. On the other hand, platinum-group catalysts, which rely on metallic platinum as an active component, exhibit excellent catalytic activity towards ORR. Yet, Pt nanoparticles are highly prone to aggregate seriously under working conditions, leading to reduced active sites and inferior stability [5]. Therefore, the rational design and facile preparation of non-noble metal electrocatalysts with cost-effectiveness, high catalytic activity, and superior stability are of paramount importance for practical applications.

Various techniques have been well developed to enhance the performance of ORR electrocatalysts, including designing single-atom active sites [6,7], doping with non-metallic heteroatoms [8,9], modifying the morphology of nanomaterials [10,11], and building multi-level nanostructures [12–14]. For example, Yamauchi et al. reported the fabrication of N-doped graphene nanomesh for anchoring iron phthalocyanine (FePc) with a well-defined Fe-N_4 coordination environment [15]. The prepared graphene nanomesh was further thermally calcined into Fe single-atom catalysts which endowed superior ORR activity in acidic media. Nonetheless, metallomacrocyclic molecules possess multi-valent redox ability as the active site for ORR owing to their adjustable *d*-orbital transition metal and symmetric conjugated ring structure [16–18], thus the preparation into a single-atom catalyst may be unnecessary [19,20]. Moreover, several reports suggest that tuning the interaction between the active species and the carriers can

* Corresponding authors.
E-mail addresses: yang201079@126.com (Z. Yang), jinjieqian@wzu.edu.cn (J. Qian).
[1] These authors contributed equally to this work.

https://doi.org/10.1016/j.apcatb.2023.123172

Available online 12 August 2023
0926-3373/© 2023 Elsevier B.V. All rights reserved.

prevent agglomeration of loaded particles, promote electron transfer, firmly anchor the metal to the carriers, and increase the stability of nanomaterials [21,22]. Therefore, designing an ideal substrate for stabilizing FePc molecules becomes a crucial step in the preparation of advanced ORR catalysts.

Microporous coordination polymers (CPs) are an emerging class of highly crystalline hybrid solids composed of metal ions/clusters and organic ligands that offer exceptional structural tunability [23–25]. For instance, Li et al. showed that the growth of Cu-based CPs with different morphologies, such as cruciate flower, cross star, and hollow dodecahedron, can be conveniently regulated through solvent-triggered methods [26]. These obtained CP materials with modified morphologies can be thermally converted into hierarchical carbon nanocomposites using various strategies, such as changing calcination temperatures and adding etching agents [27–29]. Furthermore, Xu et al. used the thermal exfoliation of one-dimensional Ni-based CP nanorods to produce two-dimensional carbon nanoribbons (CNRs) with belt-like superstructures assembled from interconnected graphitic carbon nanocages and carbon-encapsulated Ni particles immobilized on the surface, displaying excellent electrocatalytic properties [30]. Hence, selecting structurally tunable and morphologically modifiable CP precursors to fabricate desirable carbon supports for hosting active substances is a promising strategy for designing advanced electrocatalysts.

In this study, we have investigated the solvent-induced effect on the growth behavior and reversible structural interconversion of two types of In-based CPs, namely, **InOF-25** and **InOF-26**. We find that these crystals, with different morphologies and structures, can be transformed into nanostrip-shaped particles under aqueous conditions. They are suitable for synthesizing P-doped multi-defective carbon nanoribbons (**$Fe_{2P@25/26\text{-}CNR}$**) via the calcination process with the assistance of 1,1′-Bis(diphenylphosphino)ferrocene (DPPF, Scheme 1). The incorporation of P atoms acts like a nitrogen-containing species to change the electronegativity of the carbon substrate,[31–33] while the abundant defects promote the immobilization of FePc onto CNRs (**FePc-Fe_2P@25/26-CNR**). Besides, FePc can anchor onto the derived carbon substrate through π-π stacking, facilitated by the extensive conjugated aromatic system of FePc containing 18 conjugated π electrons, primarily driven by van der Waals forces [34]. The obtained **FePc--Fe_2P@25-CNR** exhibits superior ORR performance with a half-wave potential of 0.899 V and a diffusion current density of 5.152 mA cm^{-2}, attributed to the monodispersed FePc molecules, ultra-thin nanoribbon structure, and large specific surface area. Notably, the Zn-air battery with **FePc-Fe_2P@25-CNR** as the cathode shows maximum power density (115.342 mW cm^{-2} at 186.637 mA cm^{-2}) and cycling stability (100 cycles for 2000 min).

2. Experimental

2.1. Synthesis and interconversion of crystals

Firstly, **InOF-25** and **InOF-26** are synthesized by the solvothermal method, as previously reported by our group [35,36], and the yields of the obtained crystals are maintained at 85–90%. Then, **InOF-25** (30 mg) crystals are put into a glass bottle containing NMF (5 mL). Adding drops of concentrated HCl (50 μL) to this glass vial for completely dissolving the crystals. Finally, it is placed in an oven at 85 °C for 2 days, which eventually converts into **InOF-26** crystals. Similarly, the **InOF-26** (30 mg) crystals are put into a glass bottle containing DMF/EtOH (3/3 mL). The same amount of HCl is added and subjected to the same temperature and reaction time to convert into **InOF-25** crystals. The interconversion between the two crystals results in a normal loss of approximately 10%.

2.2. Synthesis of hydrolyzed products

Separately, **InOF-25** (200 mg) and **InOF-26** (200 mg) crystals are put into a beaker with H_2O (10 mL), and a stirrer is added to adjust the speed to 500 rpm for 2 days. By centrifugation and drying, the final product will be light yellow strip powders (**InOF-25-H_2O**) and white strip powders (**InOF-26-H_2O**). The yields of the two hydrolyzed products remain at 70–75%.

2.3. Synthesis of various carbon substrates

Primarily, the **InOF-25-H_2O** or **InOF-26-H_2O** powders are placed into a quartz casing which will be heated to 900 °C for 3 h under the condition of Ar gas. After cooling to room temperature, the product should be washed with 3 M HCl to remove impurities such as metal nanoparticles contained on the surface in order to obtain a clean one-dimensional carbon nanoribbon material (**25/26-CNR**). After high-temperature carbonization, most of the organic matter in various precursors undergoes thermal volatilization, resulting in carbon materials with a mass yield of approximately 25% of the precursor. To synthesize **Fe@25/26-CNR**, **InOF-25-H_2O** (100 mg) or **InOF-26-H_2O** (100 mg) are each immersed in a DMF (5 mL) solution containing ferrocene and stirred for 1 day to allow sufficient adsorption of metal salt before the carbonation process. Similarly, the polyporous carbon nanoribbons containing Fe_2P nanoparticles (**Fe_2P@25/26-CNR**) are obtained by replacing ferrocene with DPPF.

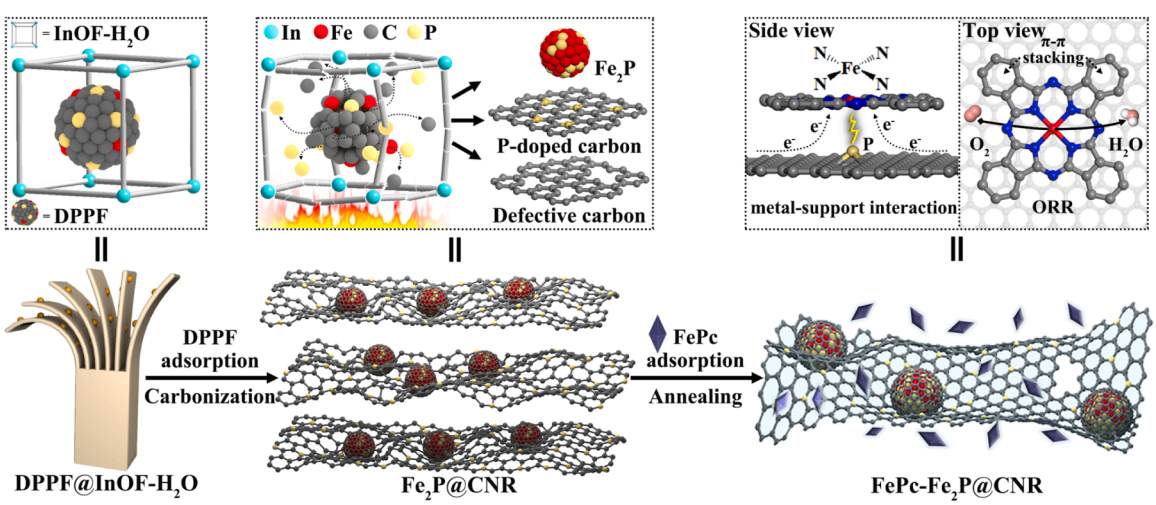

Scheme 1. The synthetic process to obtain excellent ORR electrocatalyst of **FePc-Fe_2P@25/26-CNR**.

2.4. Incorporation of FePc into carbon materials

In the final stage, all the above-synthesized carbon materials (10 mg) are loaded into DMF (5 mL) solution with FePc (5 mg) and stirred for 12 h. Subsequently, they are washed sequentially by centrifugation three times each with DMF, H_2O, and ethanol until the filtrate becomes colorless and clarified. By the centrifugation and drying processes, these mixtures are placed into a quartz casing and heated to 400 °C for 2 h under the condition of Ar gas. It is noteworthy that the structure of FePc will remain intact at 400 °C,[19] while this temperature could reinforce the binding between metallomacrocyclic and carbon substrates. Finally, it is demonstrated that FePc is successfully loaded into the as-prepared carbon composites without damaging the morphology by SEM, XRD, and Raman characterization methods.

3. Result and discussion

3.1. Spectroscopic characterizations of the structural evolution of crystals

Both In-CPs are structurally similar, consisting of equivalent inorganic building units and deprotonated isophthalic acid (BDC^{2-}), but their coordination orientations differ significantly due to the solvent-induced effect [37]. **InOF-25** has angles of BDC(I)-In-BDC(I) and BDC(II)-In-BDC (II) of 139.9° and 136.1°, respectively (Fig. 1a), with In-BDC(I)-In and In-BDC(II)-In angles of 127.6° and 112.9°, respectively, leading to anisotropic growth into a rod shape (Fig. 1b, S1a, Table S1). In contrast, the 2D bulk crystal of **InOF-26** owns angles of BDC-In-BDC (137.0°) and In-BDC-In (128.4°) in different directions, resulting in lateral growth along the *ab*-plane (Fig. 1c, S1b, Table S2). To verify the single-crystal-to-single-crystal growth manner, both In-CPs are placed into respective synthetic solutions, and the powder X-ray diffraction (PXRD) analysis confirms the high purity and crystallinity of the converted crystals (Fig. 1e, 1f). Surprisingly, they could be easily transformed into the same strip-shaped crystals (**InOF-25-H_2O** and **InOF-26-H_2O**) in the aqueous solution, indicating the critical role of water molecules in the growth of In-CPs (Fig. 1d, 1g, S2). The information about the structure of **InOF-25** and **InOF-26** after water treatment could not be determined due to the minuscule particle size, however, the similar PXRD patterns are sufficient to prove their identical structures. The specific surface area and pore structure of all crystalline materials are determined by N_2 isotherms in Fig. S3 and Table S3.

3.2. Comparison of morphologies and structures of various materials

The water-treated CPs are chosen as precursors to produce carbon

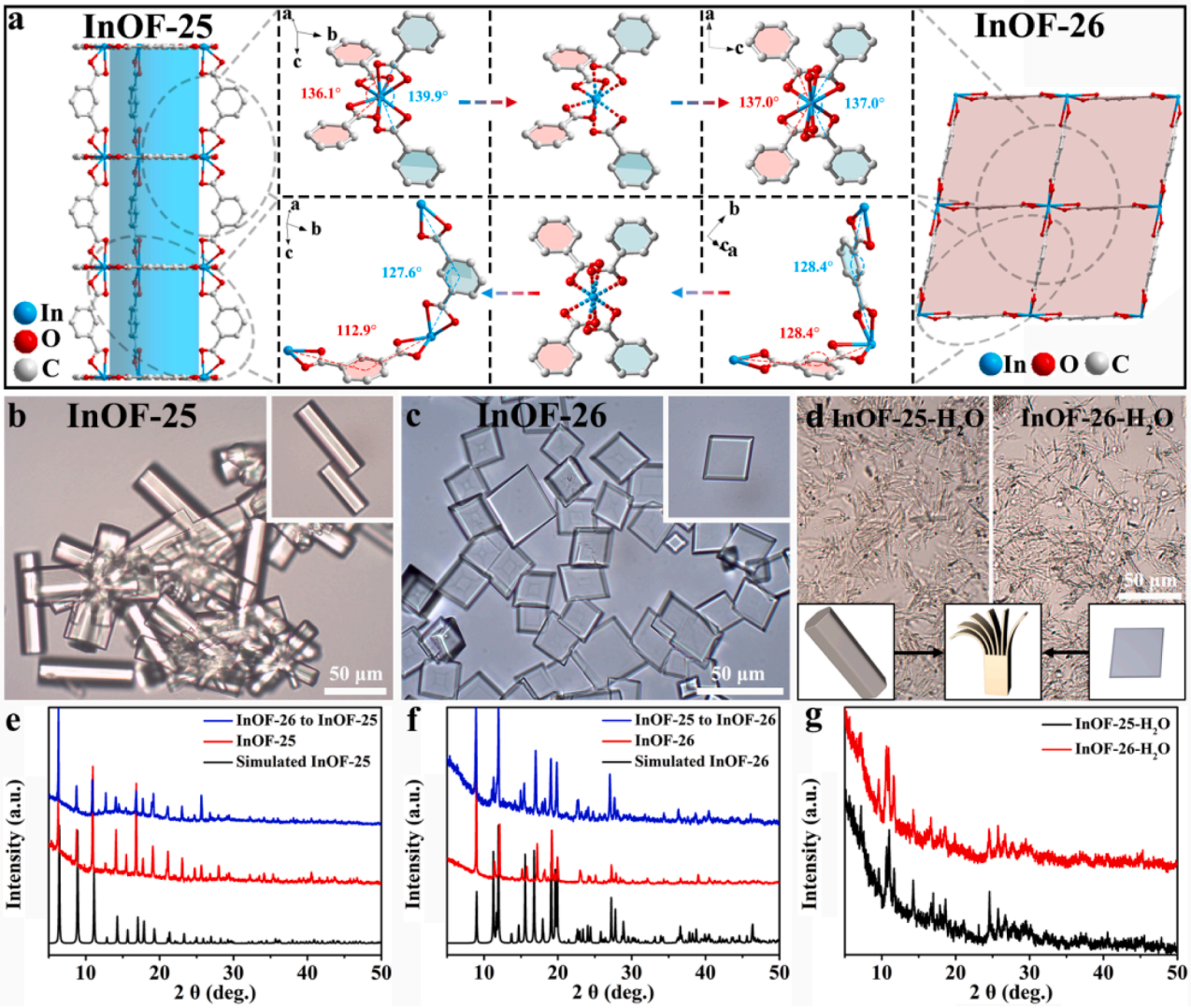

Fig. 1. a) The conversion processes and structural characteristics of two In-CPs (the blue and red benzene rings represent BDC(I) and BDC(II), respectively); b-d) Optical images and e-g) PXRD patterns of **InOF-25**, **InOF-26**, **InOF-25-H_2O**, and **InOF-26-H_2O**, respectively.

nanoribbons with highly disordered amorphous carbon through thermal transformation (**25/26-CNR**, Fig. S4). Subsequently, **Fe_2P@25-CNR** is obtained using DPPF as a pore-forming agent and P source (Fig. 2a-c). For comparison, **Fe@25-CNR** is synthesized using ferrocene by a similar method, which does not significantly alter the morphology in Fig. S5. This method is also applicable for preparing **Fe@26-CNR** and **Fe_2P@26-CNR** from **InOF-26-H_2O** (Fig. S6). The HAADF-STEM and EDS mapping reveal that **Fe_2P@25-CNR** comprises C, N, O, P, Fe, and In elements (Fig. S7), where the even distribution signifies the presence of atomically dispersed P atoms in the carbon structures. On the other hand, the characterization of the element and morphology of **25/26-CNR** and **Fe@25/26-CNR** demonstrates that the In species are almost negligible after pyrolysis and acid washing (Figs. S8, S9). The existence of carbon defects and phosphorus atoms allows stable adsorption of FePc inside or on the surface of carbon nanomaterials [38,39]. The structure and morphology of CNRs remain unchanged after doping with FePc, with no metal nanoparticles or clusters found throughout the porous nanostructures in Figs. 2d-f, S10, S11. The EDS analysis shows a significant improvement in the content of Fe and N elements with the anchoring of FePc onto CNRs (Fig. 2g, S12-S16). For **Fe_2P@25-CNR** and **FePc--Fe_2P@25-CNR**, the mass of Fe increases from 0.06 to 1.85 wt%, while the N content increases from 4.81 to 6.05 wt% (Table S4). The homogeneity of nitrogen and iron elements and the ultra-fine transition metal macrocycles can expose more active sites and increase the utilization of FeN_4 sites, thereby enhancing the subsequent electrochemical activity [40,41].

The thickness and roughness level of the synthesized carbons are further investigated using atomic force microscopy (AFM). Fig. S17a shows that the thickness of **25-CNR** ranges from 15 to 25 nm with a curled and irregular posture. In contrast, **Fe_2P@25-CNR** has an extremely small thickness (~5 nm) with a rougher surface, indicating that DPPF can effectively form ultra-thin and porous nanostructures (Fig. S17b). However, the uneven plane and larger thickness of **Fe@25/26-CNR** suggest that ferrocene only acts as an iron source during calcination (Figs. S18, S19). The obtained **FePc@25-CNR** remains smooth, and **FePc-Fe_2P@25-CNR** appears coarse, suggesting that FePc molecules can be distributed on the surface of the carbons (Fig. S17c, S17d). Similarly, the **InOF-26** series exhibit the same structural and

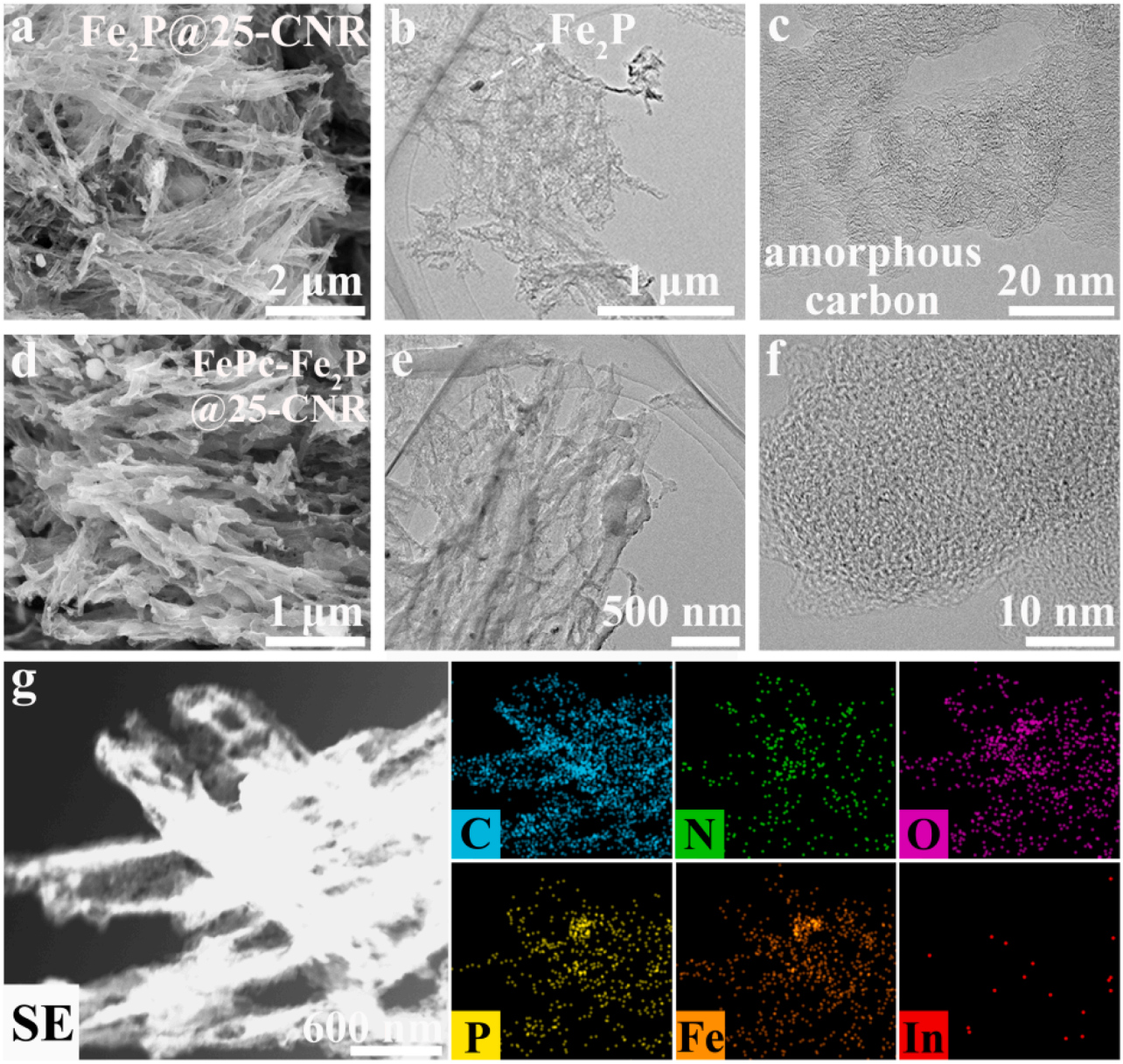

Fig. 2. The SEM, TEM, HR-TEM, and EDS mapping images of a-c) **Fe_2P@25-CNR** and d-g) **FePc-Fe_2P@25-CNR**, respectively.

morphological characteristics where **Fe_2P@26-CNR** is thinner and owns a rougher surface than **26-CNR** (Fig. S17e, S17f). The morphology and structure are hardly affected after the adsorption of FePc molecules (Fig. S17g, S17h).

The as-synthesized carbon materials are characterized for phase composition and carbon structure. There are no obvious indium/iron-related species detected for **25/26-CNR** and **Fe@25/26-CNR** (Fig. 3a, S20a). However, **Fe_2P@25/26-CNR** shows three faint diffraction peaks at 40.28°, 44.21°, and 47.28° for a few amounts of Fe_2P (PDF#51–0943). And FePc is identified with distinctive peaks at 6.87° and 9.15° for the (001) and (201) planes (Fig. 3b, S20b). **Fe_2P@25/26-CNR** displays the maximum adhesion capacity of phthalocyanines with a remarkably reduced absorption peak at 548 nm (Fig. 3c, S20c). The moderate I_D/I_G values of **Fe_2P@25-CNR** (1.033) and **Fe_2P@26-CNR** (1.060) indicate numerous disordered carbons (Figs. 3d, e, S20d, S20e). FePc molecules are successfully loaded as two emerging peaks at 679 and 1525 cm^{-1} are observed (Fig. 3f, S20f). The specific surface area and pore size distribution show that **25-CNR**, **Fe@25-CNR**, and **Fe_2P@25-CNR** have values of 778.8, 745.5, and 502.6 $m^2\ g^{-1}$, respectively, which further verifies the pore-forming role of DPPF (Fig. 3g, h, S20g, S20h, Table S3). In Fig. 3i, S20i, all the CNRs exhibit hierarchically porous nanostructures dominated by multi-pores that are favorable to enhance the electrochemically active surface area and electron/mass transfer efficiency [42,43].

X-ray photoelectron spectroscopy (XPS) is used to characterize the chemical composition and surface valence states. The full-scan spectra of **FePc-Fe_2P@25/26-CNR** show distinct C, N, O, P, Fe, and In signals when compared to control products (Fig. 4a, S21a), where most of the nitrogen originates from FePc, while phosphorus comes from DPPF. The high-resolution C 1 s spectra are classified into C-C (284.8 eV), C-N/C-P (285.8 eV), C-O (287.0 eV), and C=O (290.2 eV), where the presence of the C-P bond confirms the inclusion of P in the carbon skeleton (Fig. 4b, S21b). The O 1 s spectra show the existence of the O-P bond (530.2 eV), which is similar to the InOF-26 series carbon products (Fig. 4c, S21c). On the other hand, the O-M (531.5 eV) levels of FePc-anchored CNRs are boosted certainly, indicating that indium/iron would be partially oxidized. Meanwhile, the In $3d_{5/2}$ and $3d_{3/2}$ signal peaks at 444.5 and 452.1 eV, respectively, could be detected in Fig. S22, which originate from indium oxide (In^{3+}). The P 2p spectra also reveal the successful doping of P atoms, with three peaks assigned to P-Fe, P-C, and P-O of 130.7, 132.5, and 134.2 eV, respectively (Fig. 4d). Among them, the P-O bond is known to accelerate the charge delocalization of the adjacent C atoms and strengthen the adsorption capacity toward oxygen.[44,45] The core-level N 1 s spectrum of **FePc@25-CNR** is deconvoluted into pyridinic-N, Fe-N, pyrrolic-N, and graphitic-N in Fig. 4e, Table S6, where the Fe-N is considered to be the active center of ORR in basic electrolytes.[46,47] Meanwhile, it is believed that pyridinic-N could serve as an anchor point for Fe atoms, and the high percentage of pyridinic-N leads to the enhanced presence of Fe-N moieties. [48] The peak position of the Fe-N species of **FePc-Fe_2P@25-CNR** is shifted toward the lower binding energy (−0.1 eV), proving charge transfer between FePc and the P-doped carbon substrate. As for the Fe 2p spectra (Fig. 4f, S21f), a pair of peaks at 708.9/721.9 eV is attributed to FeN_x species, which is derived from FePc macrocyclic compound. Another

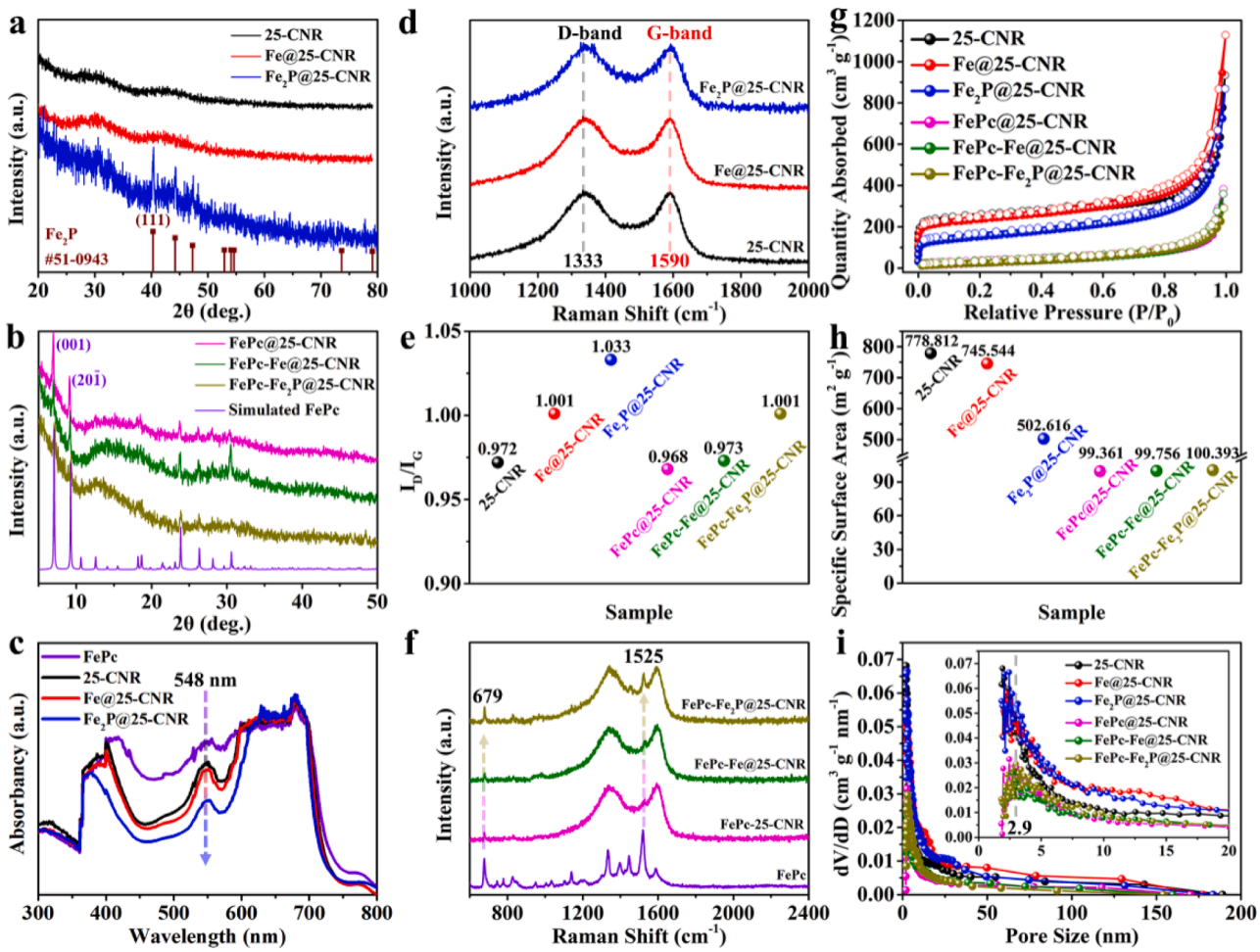

Fig. 3. a-b) PXRD patterns, c) UV-Vis spectroscopy, d-f) Raman spectra and its calculated I_D/I_G ratios, g-i) N_2 isotherms, BET specific surface areas, PSD curves of **InOF-25**-derived samples, and its inset corresponds to the region of 0–20 nm.

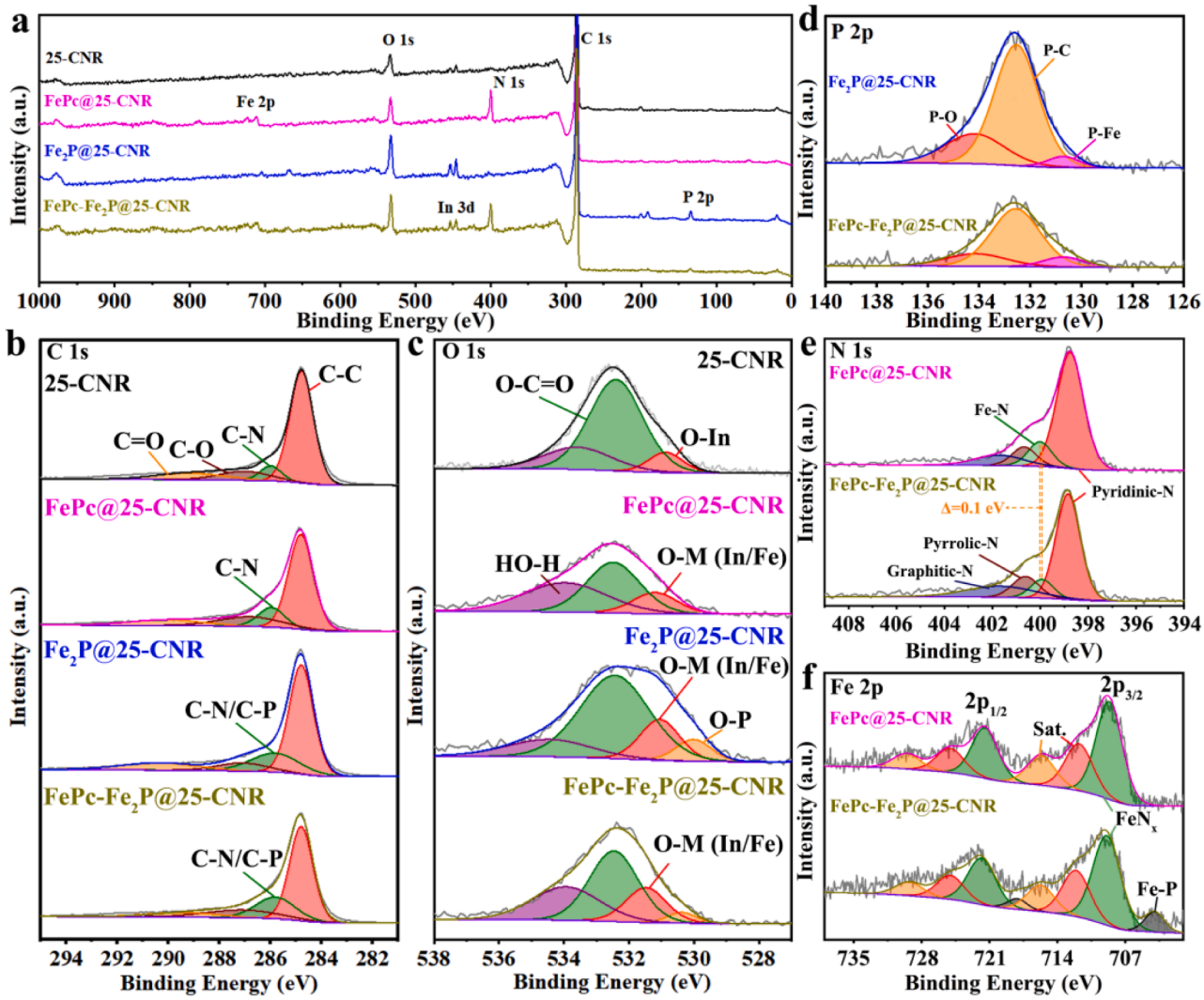

Fig. 4. a) XPS spectra, b) high-resolution C 1 s, c) O 1 s, d) P 2p, e) N 1 s, and f) Fe 2p spectra. Black, pink, blue and dark yellow lines are fitted for **25-CNR**, **FePc@25-CNR**, **Fe_2P@25-CNR**, and **FePc-Fe_2P@25-CNR**, respectively.

pair of peaks is located at 704.1 and 718.2 eV, corresponding to the Fe-P bond of the Fe_2P nanocomposite.

3.3. ORR performance of electrocatalysts

The electrocatalytic properties of CP-derived CNRs coupled with FePc are evaluated using cyclic voltammetry (CV) and linear sweep voltammetry (LSV) techniques. The CV curves reveal that **FePc-Fe_2P@25-CNR** exhibits the highest peak potential (0.916 V) among all the tested samples, which is comparable to that of Pt/C (0.943 V, Fig. S23-S25). The LSV results demonstrate that **FePc-Fe_2P@25-CNR** has the highest half-wave potential ($E_{1/2}$, 0.899 V) and diffusion-limiting current (J_L, 5.152 mA cm^{-2}), which are similar to those of Pt/C (0.874 V, 5.393 mA cm^{-2}) and superior to other FePc-based ORR catalysts in Fig. 5a, S26a, Table S7, S8. **FePc-Fe_2P@26-CNR** also exhibits superior catalytic behavior (0.901 V, 4.973 mA cm^{-2}) compared to the corresponding **InOF-26** derivatives (Fig. S26b). Moreover, the Tafel slopes for **FePc-Fe_2P@25/26-CNR** are calculated to be 30.66/39.98 mV dec^{-1}, which are significantly smaller than that of Pt/C (62.96 mV dec^{-1}) in Fig. 5c, S26c. The lower Tafel slopes (< 40 mV dec^{-1}) indicate that the decisive rate step of the oxygen reduction process is determined by the rate of consumption of OOH* species.[49] The double-layer capacitance (C_{dl}) estimated from the CV curves (Figure S27, S28) suggests that **FePc-Fe_2P@25-CNR** possesses a higher C_{dl} value (8.96 mF cm^{-2}) than **FePc-Fe@25-CNR** (4.55 mF cm^{-2}) and **FePc@25-CNR** (6.45 mF cm^{-2}) but less than **Fe_2P@25-CNR** (38.36 mF cm^{-2}), **Fe@25-CNR** (37.08 mF cm^{-2}), and **25-CNR** (31.47 mF cm^{-2}), and this trend is consistent in **InOF-26** series (Fig. 5d, S26d, Table S9). Besides, FePc-anchored CNRs also show excellent electron conductivity and smaller charge transfer resistance values, as observed in the EIS diagram, with the smaller one originating from the carbon nanoribbons and the larger one belonging to the FePc (Figs. 5e, S26e, S29). The electron transfer number (*n*) of all carbons incorporating FePc is 3.99–4.00, which is comparable to that of Pt/C (Fig. 5f, S26f). Furthermore, the Koutechy-Levich plots reveal that all products exhibit a fast first-order reaction kinetic, except for **25/26-CNR**, as evidenced by the linear relationships between 0.2 and 0.6 V (Figs. S30-S33). The long-term stability and resistance to MeOH toxicity of the catalysts in the electrocatalytic process are also investigated in Fig. S34-S38.

3.4. ZAB performance of electrocatalysts

The exceptional ORR performance of certain catalysts has led to their use as air-cathode materials in primary Zn-air batteries (ZABs). As illustrated in Fig. 6a, a homemade ZAB is constructed using a FePc-doped compound air cathode, an alkaline electrolyte, and a Zn plat anode. The two main catalysts produce voltages of 1.514 and 1.497 V, and two ZABs connected in series successfully power a commercial LED

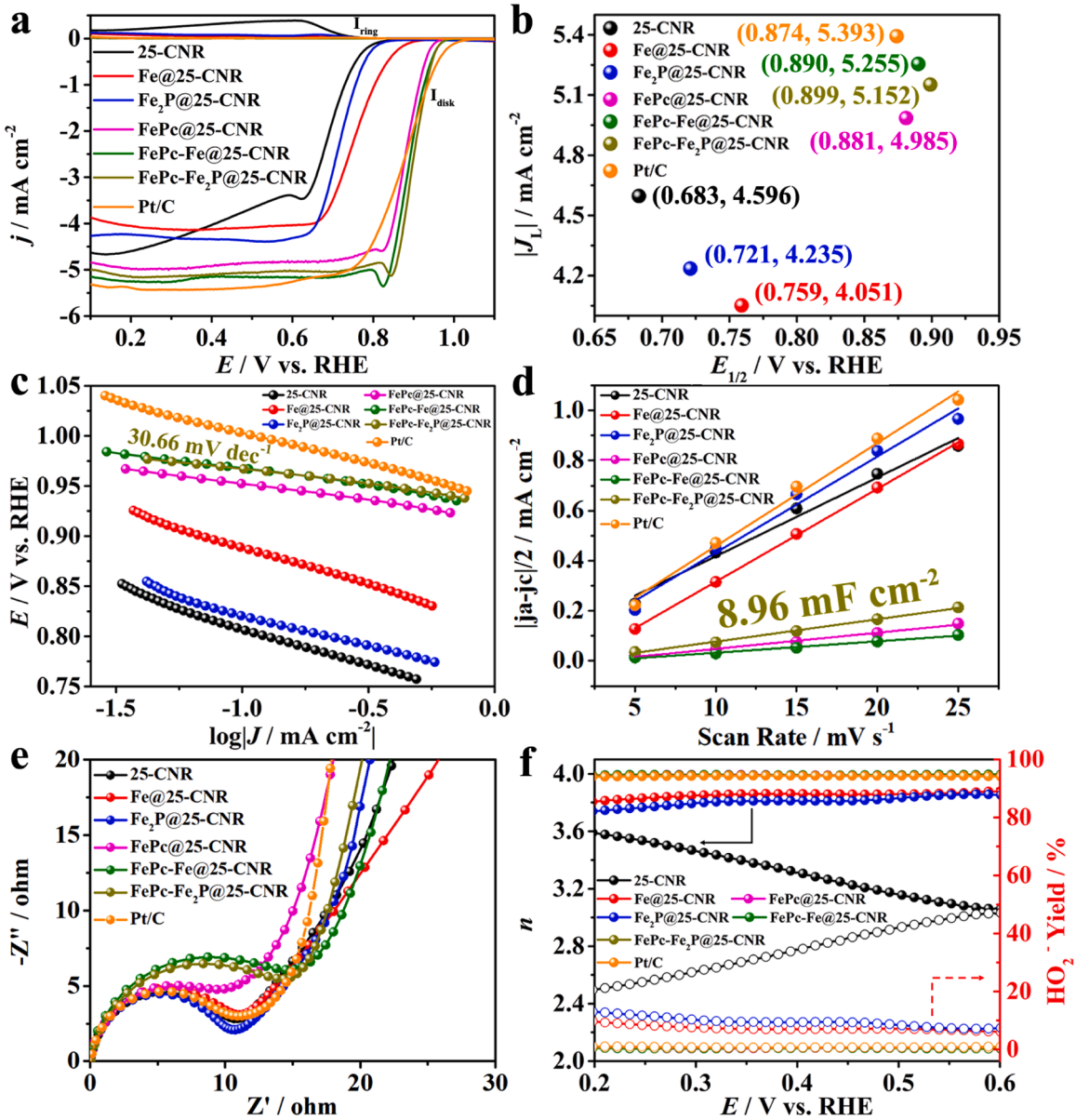

Fig. 5. a) LSV curves, b) J_L and $E_{1/2}$ values, c) Tafel slopes, d) C_{dl} lines, e) EIS plots, f) *n* and H_2O_2 yields of a series of **InOF-25**-derived samples and Pt/C, respectively.

screen, demonstrating their potential for energy devices. In open-circuit potential (OCP) measurement, the ZAB with **FePc-Fe$_2$P@25-CNR** as the cathode offers a high OCP of 1.532 V after 5 min, even surpassing that of the ZAB using the commercial Pt/C catalyst (1.513 V, Fig. 6b). In Fig. 6c, the discharge polarization and power density curves show that **FePc-Fe$_2$P@25-CNR** exhibits superior ORR behavior, with the largest current density and maximum power density (115.342 mW cm^{-2} at 186.637 mA cm^{-2}) compared to the Pt/C-based counterpart (106.901 mW cm^{-2} at 161.239 mA cm^{-2}), with all FePc-doped materials are higher than that of the Pt/C (468.060 mAh g^{-1}), with **FePc@26-CNR** reaching the best value of 571.154 mAh g^{-1}, which implies a greater utilization rate for Zn anode (Fig. 6d, Table S10). Furthermore, the ZABs display a stable voltage plateau that could be reduced and recovered with varying current density in Galvanostatic discharge measurement from 5 to 100 mA cm^{-2}, signifying the outstanding discharge stability of the battery (Fig. 6e). To further evaluate the long-term stability of the ZABs, the galvanostatic cycling test is performed at a current density of 5 mA cm^{-2} in Fig. 6f. In view of the superb oxygen reduction ability of FeN_4 species and the presence of a small amount of Fe_2P as a possible active site for oxygen evolution [50], the ZABs using Fe_2P @ CNR catalysts encapsulated with FePc present better cycling durability (**FePc-Fe$_2$P@25-CNR**: 0.94 V voltage gap and 56.1% round-trip efficiency; **FePc-Fe$_2$P@26-CNR**: 0.88 V voltage gap and 56.9% round-trip efficiency) than the Pt/C-based cell after 100 cycles for 2000 min. Overall, the results suggest that the obtained **FePc-Fe$_2$P@25/26-CNR** have great potential as efficient electrocatalysts for efficient ORR in high-efficiency ZABs.

3.5. Density functional theory calculation

To investigate the electronic interaction between the FePc molecule and P-doped carbon substrate, two model systems, FePc@PG (FePc placed on P-doped graphene) and FePc@G (FePc placed on graphene), are reasonably constructed to understand the effect of the presence of P atoms in the hybridization electron distribution (Fig. S39). As shown in Fig. 7a, after coupling with a P-doped graphene substrate, there is a noticeable electron redistribution between the graphene substrate and Fe sites. Specifically, phosphorus doping leads to an accumulation of

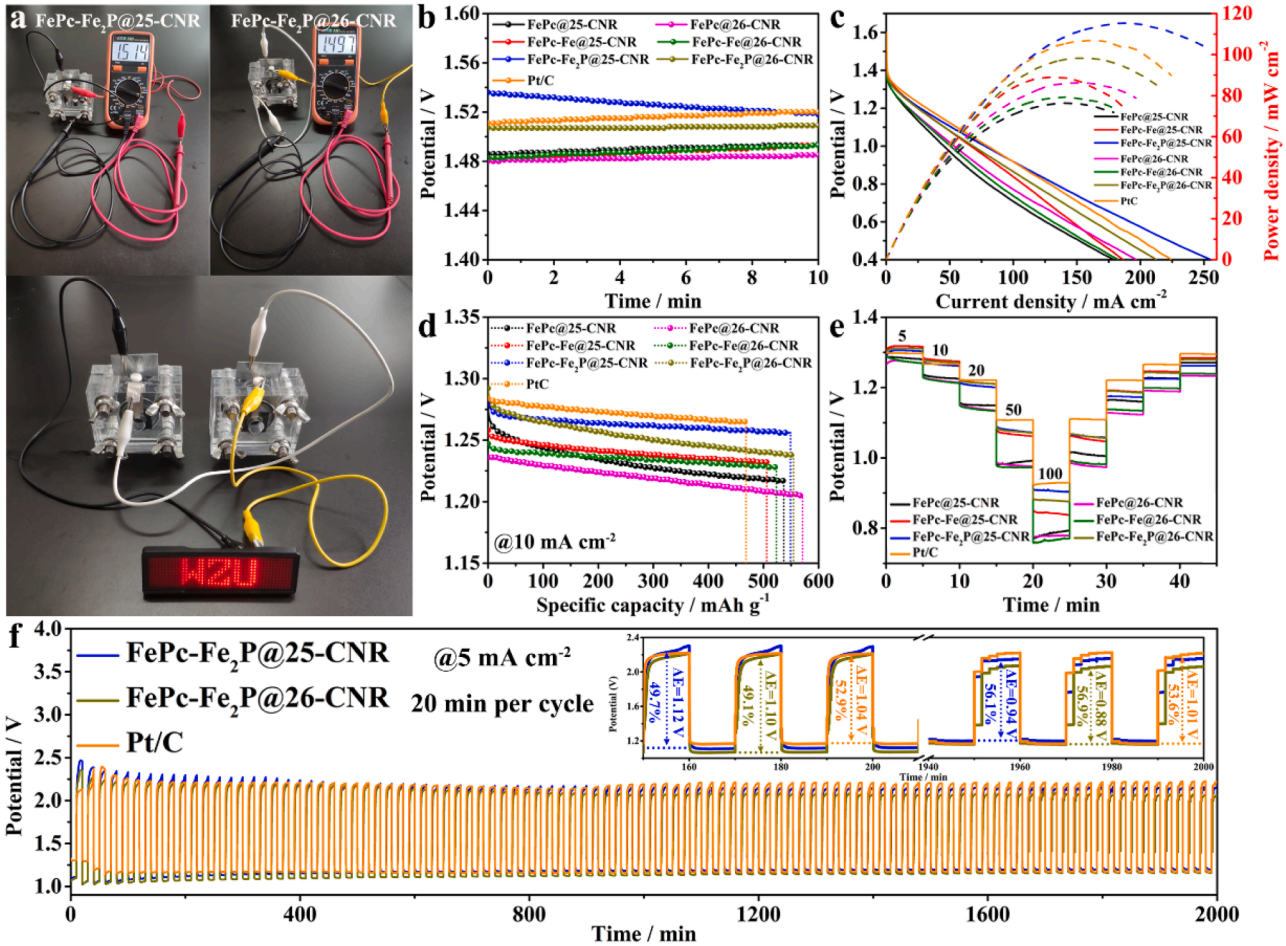

Fig. 6. a) A LED screen powered by two ZABs, b) the OCP plots, c) discharge polarization and power density, d) galvanostatic discharge curves, e) discharge curves at various current densities for a series of FePc-doped products and Pt/C, f) cycling performance of **FePc-Fe$_2$P@25/26-CNR** and Pt/C, respectively.

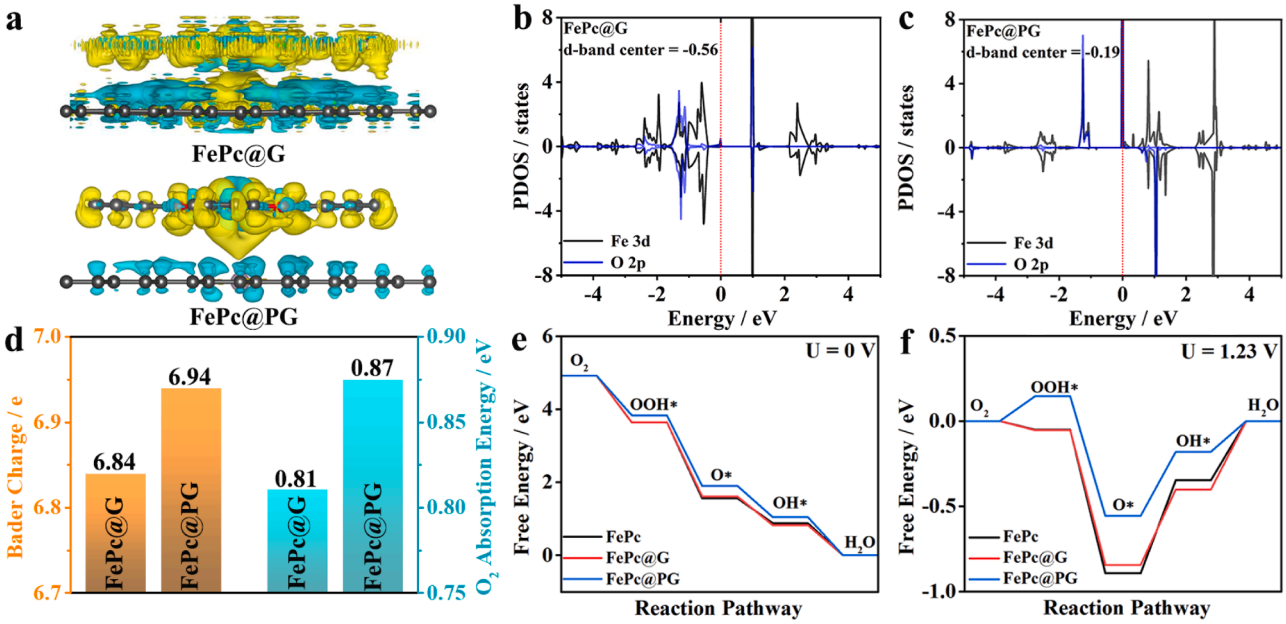

Fig. 7. a) The charge density difference of the interfaces between FePc and G/PG layers, yellow and cyan isosurfaces represent charge accumulation and depletion. b, c) the PDOS plots of FePc@G and FePc@PG, respectively, d) the Bader charge transfers and O_2 adsorption energies, and e, f) free energy diagrams of ORR pathways of FePc@G and FePc@PG.

more electrons around the Fe sites, creating electron-rich regions near the Fe sites. This accelerates the electron transfer from the Fe sites to the oxygen intermediates,[51] which is beneficial for enhancing the current density and initial potential of catalysts. Further calculations of the projected density of states (PDOS) are performed to study the electron interactions between the oxygen species and the Fe atom center after coupling with the P-doped graphene substrate. In Fig. 7b, c, FePc@PG exhibits a more positive d-band center (−0.19 eV) compared to FePc@G (−0.56 eV). The positive shift in the d-band center implies that more antibonding orbitals are located above the Fermi level, resulting in a higher proportion of bonding orbitals in the Fe-O_2 adsorption system and stabilizing the adsorption system. Meanwhile, it is illustrated that the central Fe atom of FePc@PG possesses more Bader charge, indicating that the P-doped graphene substrate transfers more electrons to FePc, which is consistent with the previous differential charge analysis (Fig. 7d). The adsorption energy of O_2 on FePc@G and FePc@PG is also calculated, and it is evident that FePc@PG exhibits higher adsorption energy for O_2, consistent with the earlier PDOS analysis. Furthermore, the free energy change diagrams for FePc, FePc@G, and FePc@PG during the ORR process are also calculated. At U = 0 V, all electron transfer steps are thermodynamically spontaneous, and all three materials show the lowest ΔG in the transition from O* -OH* (Fig. 7e). Among them, FePc@PG exhibits the largest ΔG (0.853 eV) compared to FePc and FePc@G (0.683 and 0.786 eV), indicating its ability to provide a higher potential during the ORR process. At U = 1.23 V, the rate-determining step for all three is still the O* -OH* step, and FePc@PG shows the lowest energy barrier 0.370 eV, compared to FePc and FePc@G (0.547 and 0.444 eV, Fig. 7f). Overall, when using the P-doped graphene to anchor FePc, the ORR performance of the material is attributed: 1) A higher O_2 adsorption energy, which enhances the intrinsic activity of the material; 2) The phosphorus-doped graphene substrate transfers more electrons to FePc, creating electron-rich regions in the Fe center, making it easier for electrons to transfer from Fe to the adsorbed intermediates, favoring the formation of OH* .

4. Conclusion

To summarize, we have explored the role of solvent-induced effects in converting two isotropic In-based CPs into tripe-like grains with the same structure in an aqueous environment. These grains are then used as precursors to synthesize phosphorus-doped ultra-thin carbon nanoribbons with multi-level defects for effectively anchoring FePc. The presence of abundant defects provides a large number of active sites to capture oxygen-related species more easily, while the doping of phosphorus atoms results in a carbon substrate with electronegativity not only to improve the association with FePc through metal-support interaction, but also to realize the fast electron migration. The resulting electrocatalysts of **FePc-Fe_2P@25/26-CNR** show excellent ORR performance with a high onset potential, half-wave potential, and large diffusion current density in alkaline solution. The exceptional cycling stability of ZABs assembled with these electrocatalysts as cathode materials could be reasonably attributed to the robust and multi-porous carbon nanoribbon structure that firmly anchors the active substances. Finally, these findings highlight the potential of CP-derived carbon nanoribbons as porous carriers for loading active substances toward efficient energy storage.

CRediT authorship contribution statement

Jinjie Qian provided the idea for this work, designed relevant experiments, analyzed experiment results, and revised the manuscript. **Qi Huang** prepared and characterized the samples, performed relevant electrochemical performance tests, analyzed experiment results, and composed the manuscript. **Shaojie Xu** and **Jie Liu** equally contributed to the syntheses and theoretical calculations. **Yuanyuan Guo**, **Dandan Chen**, **Qiuhong Sun**, **Linjie Zhang**, **Huagui Nie**, and **Zhi Yang** provided great assistance during the experimental process. All authors have reviewed and approved the final version of the manuscript.

Declaration of Competing Interest

The authors declare that they have no known competing financial interests or personal relationships that could have appeared to influence the work reported in this paper.

Data Availability

Data will be made available on request.

Acknowledgements

This work was financially supported by National Natural Science Foundation of China (21601137), Natural Science Foundation of Zhejiang Province (LQ16B010003), Basic Science and Technology Research Project of Wenzhou, Zhejiang Province (H20220001), the State Key Laboratory of Structural Chemistry, Chinese Academy of Sciences (20190008), and the Special Basic Cooperative Research Programs of Yunnan Provincial Undergraduate Universities Association (202101BA070001-042).

Appendix A. Supporting information

Supplementary data associated with this article can be found in the online version at doi:10.1016/j.apcatb.2023.123172.

References

[1] L. An, T.S. Zhao, Y.S. Li, Carbon-neutral sustainable energy technology: direct ethanol fuel cells, Renew. Sust. Energy Rev. 50 (2015) 1462–1468, https://doi.org/10.1016/j.rser.2015.05.074.
[2] T. Asset, P. Atanassov, Iron-nitrogen-carbon catalysts for proton exchange membrane fuel cells, Joule 4 (2020) 33–44, https://doi.org/10.1016/j.joule.2019.12.002.
[3] L.J. Yang, J.L. Shui, L. Du, Y.Y. Shao, J. Liu, L.M. Dai, Z. Hu, Carbon-based metal-free ORR electrocatalysts for fuel cells: past, present, and future, Adv. Mater. 31 (2019), 1804799, https://doi.org/10.1002/adma.201804799.
[4] L. Yang, X.F. Zeng, W.C. Wang, D.P. Cao, Recent progress in MOF-derived, heteroatom-doped porous carbons as highly efficient electrocatalysts for oxygen reduction reaction in fuel cells, Adv. Funct. Mater. 28 (2018), 1704537, https://doi.org/10.1002/adfm.201704537.
[5] Z.X. Wu, Y.Y. Lv, Y.Y. Xia, P.A. Webley, D.Y. Zhao, Ordered mesoporous platinum@graphitic carbon embedded nanophase as a highly active, stable, and methanol-tolerant oxygen reduction electrocatalyst, J. Am. Chem. Soc. 134 (2012) 2236–2245, https://doi.org/10.1021/ja209753w.
[6] C.Z. Zhu, Q.R. Shi, B.Z. Xu, S.F. Fu, G. Wan, C. Yang, S.Y. Yao, J.H. Song, H. Zhou, D. Du, S.P. Beckman, D. Su, Y.H. Lin, Hierarchically porous M-N-C (M = Co and Fe) single-atom electrocatalysts with robust MN_x active moieties enable enhanced ORR performance, Adv. Energy Mater. 8 (2018), 1801956, https://doi.org/10.1002/aenm.201801956.
[7] X.P. Han, X.F. Ling, Y. Wang, T.Y. Ma, C. Zhong, W.B. Hu, Y.D. Deng, Generation of nanoparticle, atomic-cluster, and single-atom cobalt catalysts from zeolitic imidazole frameworks by spatial isolation and their use in zinc-air batteries, Angew. Chem. Int. Ed. 131 (2019) 5413–5418, https://doi.org/10.1002/ange.201901109.
[8] Y.J. Chen, S.F. Ji, Y.G. Wang, J.C. Dong, W.X. Chen, Z. Li, R.A. Shen, L.R. Zheng, Z. B. Zhuang, D.S. Wang, Y.D. Li, Isolated single iron atoms anchored on N-doped porous carbon as an efficient electrocatalyst for the oxygen reduction reaction, Angew. Chem. Int. Ed. 56 (2017) 6937–6941, https://doi.org/10.1002/anie.201702473.
[9] J. Quílez-Bermejo, M. Melle-Franco, E. San-Fabián, E. Morallón, D. Cazorla-Amorós, Towards understanding the active sites for the ORR in N-doped carbon materials through fine-tuning of nitrogen functionalities: an experimental and computational approach, J. Mater. Chem. A 7 (2019) 24239–24250, https://doi.org/10.1039/C9TA07932G.
[10] X. Wang, A.R. Dong, Z.Y. Zhu, L.L. Chai, J.Y. Ding, L. Zhong, T.-T. Li, Y. Hu, J. J. Qian, S.M. Huang, Surfactant-mediated morphological evolution of MnCo prussian blue structures, Small 16 (2020), 2004614, https://doi.org/10.1002/smll.202004614.
[11] J.J. Ban, X.H. Wen, H.J. Xu, Z. Wang, X.H. Liu, G.Q. Cao, G.S. Shao, J.H. Hu, Dual evolution in defect and morphology of single-atom dispersed carbon based oxygen electrocatalyst, Adv. Funct. Mater. 31 (2021), 2010472, https://doi.org/10.1002/adfm.202010472.

[12] D.N. Ding, K. Shen, X.D. Chen, H.R. Chen, J.Y. Chen, T. Fan, R.F. Wu, Y.W. Li, Multi-level architecture optimization of MOF-templated Co-based nanoparticles embedded in hollow N-doped carbon polyhedra for efficient OER and ORR, ACS Catal. 8 (2018) 7879–7888, https://doi.org/10.1021/acscatal.8b02504.

[13] L.L. Chai, J.Q. Pan, Y. Hu, J.J. Qian, M.C. Hong, Rational design and growth of MOF-on-MOF heterostructures, Small 17 (2021), 2100607, https://doi.org/10.1002/smll.202100607.

[14] E. Proietti, F. Jaouen, M. Lefèvre, N. Larouche, J. Tian, J. Herranz, J.-P. Dodelet, Iron-based cathode catalyst with enhanced power density in polymer electrolyte membrane fuel cells, Nat. Commun. 2 (2011), 416, https://doi.org/10.1038/ncomms1427.

[15] J.J. Li, W. Xia, J. Tang, Y. Gao, C. Jiang, Y.N. Jia, T. Chen, Z.F. Hou, R.J. Qi, D. Jiang, T. Asahi, X.T. Xu, T. Wang, J.P. He, Y. Yamauchi, Metal-organic framework-derived graphene mesh: a robust scaffold for highly exposed Fe-N_4 active sites toward an excellent oxygen reduction catalyst in acid media, J. Am. Chem. Soc. 144 (2022) 9280–9291, https://doi.org/10.1021/jacs.2c00719.

[16] R. JASINSKI, A new fuel cell cathode catalyst, Nature 201 (1964) 1212–1213, https://doi.org/10.1038/2011212a0.

[17] J.H. Zagal, M.T.M. Koper, Reactivity descriptors for the activity of molecular MN4 catalysts for the oxygen reduction reaction, Angew. Chem. Int. Ed. 55 (2016) 14510–14521, https://doi.org/10.1002/anie.201604311.

[18] C.Z. Loyola, S. Ureta-Zañartu, J.H. Zagal, F. Tasca, Activity volcano plots for the oxygen reduction reaction using FeN4 complexes: from reported experimental data to the electrochemical meaning, Curr. Opin. Electro 32 (2022), 100923, https://doi.org/10.1016/j.coelec.2021.100923.

[19] Y.Y. Jiang, Y.Z. Lu, X.Y. Lv, D.X. Han, Q.X. Zhang, L. Niu, W. Chen, Enhanced catalytic performance of Pt-free iron phthalocyanine by graphene support for efficient oxygen reduction reaction, ACS Catal. 3 (2013) 1263–1271, https://doi.org/10.1021/cs4001927.

[20] J. Yang, F. Toshimitsu, Z. Yang, T. Fujigaya, N. Nakashima, Pristine carbon nanotube/iron phthalocyanine hybrids with a well-defined nanostructure show excellent efficiency and durability for the oxygen reduction reaction, J. Mater. Chem. A 5 (2017) 1184–1191, https://doi.org/10.1039/C6TA07882F.

[21] Z.P. Zhang, M.L. Dou, J. Ji, F. Wang, Phthalocyanine tethered iron phthalocyanine on graphitized carbon black as superior electrocatalyst for oxygen reduction reaction, Nano Energy 34 (2017) 338–343, https://doi.org/10.1016/j.nanoen.2017.02.042.

[22] X.Z. Yu, S.J. Lai, S.S. Xin, S. Chen, X.L. Zhang, X.L. She, T.R. Zhan, X.L. Zhao, D. J. Yang, Coupling of iron phthalocyanine at carbon defect site via π-π stacking for enhanced oxygen reduction reaction, Appl. Catal. B-Environ. 280 (2021), 119437, https://doi.org/10.1016/j.apcatb.2020.119437.

[23] M. Tran, K. Kline, Y. Qin, Y.X. Shen, M.D. Green, S. Tongay, 2D coordination polymers: design guidelines and materials perspective, Appl. Phys. Rev. 6 (2019), 041311, https://doi.org/10.1063/1.5110895.

[24] L. Zhong, J.Y. Ding, J.J. Qian, M.C. Hong, Unconventional inorganic precursors determine the growth of metal-organic frameworks, Coord. Chem. Rev. 434 (2021), 213804, https://doi.org/10.1016/j.ccr.2021.213804.

[25] Y. Yang, Q. Huang, Q. Sun, J. Xue, S. Xu, L. Mao, X. Zhou, D. Yu, Q. Li, J. Qian, Fe-induced coordination environment regulation in MOF-derived carbon materials for oxygen reduction, ACS Sustain. Chem. Eng. 10 (2022) 8641–8649, https://doi.org/10.1021/acssuschemeng.2c02451.

[26] L. He, W. Li, Z.W. Jiang, T.T. Zhao, Y. Li, C.M. Li, C.Z. Huang, Y.F. Li, Novel solvent-triggered transformation of Cu-based metal-organic gels to highly monodisperse metal-organic frameworks with controllable shapes, Chem. Eng. J. 374 (2019) 1231–1240, https://doi.org/10.1016/j.cej.2019.06.026.

[27] K.J. Lee, J.H. Lee, S. Jeoung, H.R. Moon, Transformation of metal-organic frameworks/coordination polymers into functional nanostructured materials: experimental approaches based on mechanistic insights, Acc. Chem. Res. 50 (2017) 2684–2692, https://doi.org/10.1021/acs.accounts.7b00259.

[28] B.Y. Guan, A. Kushima, L. Yu, S. Li, J. Li, X.W. (David) Lou, Coordination polymers derived general synthesis of multishelled mixed metal-oxide particles for hybrid supercapacitors, Adv. Mater. 29 (2017), 1605902, https://doi.org/10.1002/adma.201605902.

[29] L. Tong, L.L. Zhang, Y.C. Wang, L.Y. Wan, Q.Q. Yan, C. Hua, C.J. Jiao, Z.Y. Zhou, Y. W. Ding, B. Liu, H.W. Liang, Hierarchically porous carbons derived from nonporous coordination polymers, ACS Appl. Mater. Interfaces 12 (2020) 25211–25220, https://doi.org/10.1021/acsami.0c06423.

[30] R.C. Wei, Y. Gu, L.L. Zou, B.J. Xi, Y.X. Zhao, Y.N. Ma, Y.T. Qian, S.L. Xiong, Q. Xu, Nanoribbon superstructures of graphene nanocages for efficient electrocatalytic hydrogen evolution, Nano Lett. 20 (2020) 7342–7349, https://doi.org/10.1021/acs.nanolett.0c02766.

[31] R.G. Cao, R. Thapa, H. Kim, X.D. Xu, M.G. Kim, Q. Li, N. Park, M.L. Liu, J. Cho, Promotion of oxygen reduction by a bio-inspired tethered iron phthalocyanine carbon nanotube-based catalyst, Nat. Commun. 4 (2013), 2076, https://doi.org/10.1038/ncomms3076.

[32] C.Z. Loyola, G. Abarca, S. Ureta-Zañartu, C. Aliaga, J.H. Zagal, M.T. Sougrati, F. Jaouen, W. Orellana, F. Tasca, Insights into the electronic structure of Fe penta-coordinated complexes. Spectroscopic examination and electrochemical analysis for the oxygen reduction and oxygen evolution reactions, J. Mater. Chem. A 9 (2021) 23802–23816, https://doi.org/10.1039/D1TA05991B.

[33] J. Barrio, A. Pedersen, S.Ch Sarma, A. Bagger, M.J. Gong, S. Favero, C.-X. Zhao, R. Garcia-Serres, A.Y. Li, Q. Zhang, F. Jaouen, F. Maillard, A. Kucernak, I.E. L. Stephens, M.-M. Titirici, FeNC oxygen reduction electrocatalyst with high utilization penta-coordinated sites, Adv. Mater. 35 (2023), 2211022, https://doi.org/10.1002/adma.202211022.

[34] Z.-Y. Mei, S. Cai, G.F. Zhao, X.X. Zou, Y. Fu, J.W. Jiang, Q. An, M. Li, T.T. Liu, H. Guo, Boosting the ORR active and Zn-air battery performance through ameliorating the coordination environment of iron phthalocyanine, Chem. Eng. J. 430 (2022), 132691, https://doi.org/10.1016/j.cej.2021.132691.

[35] Q. Huang, Y.Y. Guo, D.D. Chen, L.J. Zhang, T.T. Li, Y. Hu, J.J. Qian, S.M. Huang, Rational construction of ultrafine noble metals onto carbon nanoribbons with efficient oxygen reduction in practical alkaline fuel cell, Chem. Eng. J. 424 (2021), 130336, https://doi.org/10.1016/j.cej.2021.130336.

[36] Q. Huang, Y.W. Xu, Y.Y. Guo, L.J. Zhang, Y. Hu, J.J. Qian, S.M. Huang, Highly graphitized N-doped carbon nanosheets from 2-dimensional coordination polymers for efficient metal-air batteries, Carbon 188 (2022) 135–145, https://doi.org/10.1016/j.carbon.2021.11.062.

[37] T. Kundu, M. Wahiduzzaman, B.B. Shah, G. Maurin, D. Zhao, Solvent-induced control over breathing behavior in flexible metal-organic frameworks for natural-gas delivery, Angew. Chem. Int. Ed. 58 (2019) 8073–8077, https://doi.org/10.1002/anie.201902738.

[38] W.Z. Cheng, Pe.F. Yuan, Z.R. Lv, Y.Y. Guo, Y.Y. Qiao, X.Y. Xue, X. Liu, W.L. Bai, K. X. Wang, Q. Xu, J.N. Zhang, Boosting defective carbon by anchoring well-defined atomically dispersed metal-N_4 sites for ORR, OER, and Zn-air batteries, Appl. Catal. B-Environ. 260 (2020), 118198, https://doi.org/10.1016/j.apcatb.2019.118198.

[39] K. Yuan, D. Lützenkirchen-Hecht, L.B. Li, L. Shuai, Y.Z. Li, R. Cao, M. Qiu, X. D. Zhuang, M.K.H. Leung, Y.W. Chen, U. Scherf, Boosting oxygen reduction of single iron active sites via geometric and electronic engineering: nitrogen and phosphorus dual coordination, J. Am. Chem. Soc. 142 (2020) 2404–2412, https://doi.org/10.1021/jacs.9b11852.

[40] X. Wan, X.F. Liu, Y.C. Li, R.H. Yu, L.R. Zheng, W.S. Yan, H. Wang, M. Xu, J.L. Shui, Fe-N-C electrocatalyst with dense active sites and efficient mass transport for high-performance proton exchange membrane fuel cells, Nat. Catal. 2 (2019) 259–268, https://doi.org/10.1038/s41929-019-0237-3.

[41] J.D. Yi, R. Xu, Q. Wu, T. Zhang, K.T. Zang, J. Luo, Y.L. Liang, Y.B. Huang, R. Cao, Atomically dispersed iron-nitrogen active sites within porphyrinic triazine-based frameworks for oxygen reduction reaction in both alkaline and acidic media, ACS Energy Lett. 3 (2018) 883–889, https://doi.org/10.1021/acsenergylett.8b00245.

[42] Q. Sun, K. Zhu, X. Ji, D. Chen, C. Han, T. Li, Y. Hu, S. Huang, J. Qian, MOF-derived three-dimensional ordered porous carbon nanomaterial for efficient alkaline zinc-air batteries, Sci. China Mater. 65 (2022) 1453–1462, https://doi.org/10.1007/s40843-021-1933-4.

[43] X.F. Lu, B.Y. Xia, S.Q. Zang, X.W. (David) Lou, Metal-organic frameworks based electrocatalysts for the oxygen reduction reaction, Angew. Chem. Int. Ed. 132 (2020) 4662–4678, https://doi.org/10.1002/ange.201910309.

[44] L.L. Chen, Y.L. Zhang, L.L. Dong, X.J. Liu, L. Long, S.Y. Wang, C.Y. Liu, S.J. Dong, J. B. Jia, Honeycomb-like 3D N-, P-codoped porous carbon anchored with ultrasmall Fe_2P nanocrystals for efficient Zn-air battery, Carbon 158 (2020) 885–892, https://doi.org/10.1016/j.carbon.2019.11.073.

[45] R. Ma, X. Cui, X.X. Xu, Y.L. Wang, G.Q. Xiang, L.K. Gao, Z.Q. Lin, Y.K. Yang, Collaborative integration of ultrafine Fe_2P nanocrystals into Fe, N, P-codoped carbon nanoshells for highly-efficient oxygen reduction, Nano Energy 108 (2023), 108179, https://doi.org/10.1016/j.nanoen.2023.108179.

[46] Y.J. Sa, D.-J. Seo, J. Woo, J.T. Lim, J.Y. Cheon, S.Y. Yang, J.M. Lee, D. Kang, T. J. Shin, H.S. Shin, H.Y. Jeong, C.S. Kim, M.G. Kim, T.-Y. Kim, S.H. Joo, A general approach to preferential formation of active Fe-N_x sites in Fe-N/C electrocatalysts for efficient oxygen reduction reaction, J. Am. Chem. Soc. 138 (2016) 15046–15056, https://doi.org/10.1021/jacs.6b09470.

[47] Y.Y. Meng, D. Voiry, A. Goswami, X.X. Zou, X.X. Huang, M. Chhowalla, Z.W. Liu, T. Asefa, N-, O-, and S-tridoped nanoporous carbons as selective catalysts for oxygen reduction and alcohol oxidation reactions, J. Am. Chem. Soc. 136 (2014) 13554–13557, https://doi.org/10.1021/ja507463w.

[48] J.P. Wang, G.K. Han, L.G. Wang, L. Du, G.Y. Chen, Y.Z. Gao, Y.L. Ma, C.Y. Du, X. Q. Cheng, P.J. Zuo, G.P. Yin, ZIF-8 with ferrocene encapsulated: a promising precursor to single-atom Fe embedded nitrogen-doped carbon as highly efficient catalyst for oxygen electroreduction, Small 14 (2018), 1704282, https://doi.org/10.1002/smll.201704282.

[49] T. Shinagawa, A.T. Garcia-Esparza, K. Takanabe, Insight on Tafel slopes from a microkinetic analysis of aqueous electrocatalysis for energy conversion, Sci. Rep. 5 (2015), 13801, https://doi.org/10.1038/srep13801.

[50] P.F. Liu, X. Li, S. Yang, M.Y. Zu, P. Liu, B. Zhang, L.R. Zheng, H.J. Zhao, H.G. Yang, $Ni_2P(O)/Fe_2P(O)$ interface can boost oxygen evolution electrocatalysis, ACS Energy Lett. 2 (2017) 2257–2263, https://doi.org/10.1021/acsenergylett.7b00638.

[51] K.J. Chen, K. Liu, P.D. An, H.J.W. Li, Y.Y. Lin, J.H. Hu, C.K. Jia, J.W. Fu, H.M. Li, H. Liu, Z. Lin, W.Z. Li, J.H. Li, Y.R. Lu, T.S. Chan, N. Zhang, M. Liu, Iron phthalocyanine with coordination induced electronic localization to boost oxygen reduction reaction, Nat. Commun. 11 (2020), 4173, https://doi.org/10.1038/s41467-020-18062-y.